

# REPORT DOCUMENTATION PAGE

Form Approved  
OMB No. 0704-0188

The public reporting burden for this collection of information is estimated to average 1 hour per response, including the time for reviewing instructions, searching existing data sources, gathering and maintaining the data needed, and completing and reviewing the collection of information. Send comments regarding this burden estimate or any other aspect of this collection of information, including suggestions for reducing the burden, to Department of Defense, Washington Headquarters Services, Directorate for Information Operations and Reports (0704-0188), 1215 Jefferson Davis Highway, Suite 1204, Arlington, VA 22202-4302. Respondents should be aware that notwithstanding any other provision of law, no person shall be subject to any penalty for failing to comply with a collection of information if it does not display a currently valid OMB control number.

PLEASE DO NOT RETURN YOUR FORM TO THE ABOVE ADDRESS.

1. REPORT DATE (DD-MM-YYYY) 15-06-2004		2. REPORT TYPE Reprint		3. DATES COVERED (From - To)	
4. TITLE AND SUBTITLE Estimating the amplitude scintillation index from sparsely sampled phase screen data				5a. CONTRACT NUMBER	
				5b. GRANT NUMBER	
				5c. PROGRAM ELEMENT NUMBER 61102F	
6. AUTHOR(S) T. L. Beach T. R. Pedersen M.J. Strks				5d. PROJECT NUMBER 2311	
				5e. TASK NUMBER RS	
				5f. WORK UNIT NUMBER A1	
7. PERFORMING ORGANIZATION NAME(S) AND ADDRESS(ES) Air Force Research Laboratory/VSBXI 29 Randolph Road Hanscom AFB, MA 01731-3010				8. PERFORMING ORGANIZATION REPORT NUMBER AFRL-VS-HA-TR-2004-1203	
9. SPONSORING/MONITORING AGENCY NAME(S) AND ADDRESS(ES)				10. SPONSOR/MONITOR'S ACRONYM(S)	
				11. SPONSOR/MONITOR'S REPORT NUMBER(S)	
12. DISTRIBUTION/AVAILABILITY STATEMENT Approved for public release; distribution unlimited					
13. SUPPLEMENTARY NOTES Reprinted from Radio Science, Voil. 39, RS5001, doi:10.1029/2002RS002792, 2004					
14. ABSTRACT Phase screen techniques are commonly used to model scintillation of radio signals passing through a disturbed ionosphere, but observational phase or in situ density from both archival and real-time sources is often sampled at rates well below the resolution desired. Previous phase screen resolution criteria do not address the computation of the amplitude scintillation index (S4), which is widely used in scintillation monitoring systems, for practical applications that rely on coarsely sampled phase data. We investigate the accuracy of S4 estimates from sparsely probed one-dimensional phase screen models through systematic removal of samples from high-resolution discrete phase screen models in novel numerical experiments. We also provide analytic approximation for the weak-scatter case and study the effects of antialias filtering. This "subsampling" analysis shows that 2-5 samples per Fresnel radius (rF) are usually sufficient to compute S4 to within 90% of its true value, depending on the form of the phase spectral density function (SDF) and the strength of scattering. We make initial application of the subsampling techniques to data-based phase screens for studying equatorial ionospheric scintillation with generally satisfactory results. Finally, we outline the use of the techniques developed in this paper to other practical problems, including SDF determination and computing irradiance patterns.					
15. SUBJECT TERMS Scatterina and diffraction      Equatorial ionosphere      Ionospheric irregularities      Wave propagation Space and satellite communications      Phase screen      Scintillation					
16. SECURITY CLASSIFICATION OF:			17. LIMITATION OF ABSTRACT  UNL	18. NUMBER OF PAGES	19a. NAME OF RESPONSIBLE PERSON Theodore L. Beach
a. REPORT UNCL	b. ABSTRACT UNCL	c. THIS PAGE UNCL			19b. TELEPHONE NUMBER (Include area code) 781 377-8767

20041227 007

## Estimating the amplitude scintillation index from sparsely sampled phase screen data

T. L. Beach, T. R. Pedersen, and M. J. Starks

Air Force Research Laboratory, Space Vehicles Directorate, Hanscom Air Force Base, Massachusetts, USA

S.-Y. Su

Institute of Space Science and Center for Space and Remote Sensing Research, National Central University, Chung-Li, Taiwan

Received 4 October 2002; revised 1 June 2004; accepted 15 June 2004; published 1 September 2004.

[1] Phase screen techniques are commonly used to model scintillation of radio signals passing through a disturbed ionosphere, but observational phase or in situ density from both archival and real-time sources is often sampled at rates well below the resolution desired for input to such models. Previous phase screen resolution criteria do not address the computation of the amplitude scintillation index ( $S_4$ ), which is widely used in scintillation monitoring systems, for practical applications that rely on coarsely sampled phase data. We investigate the accuracy of  $S_4$  estimates from sparsely populated one-dimensional phase screen models through systematic removal of samples from high-resolution discrete phase screen models in novel numerical experiments. We also provide analytic approximations for the weak-scatter case and study the effects of antialias filtering. This "subsampling" analysis shows that 2–5 samples per Fresnel radius ( $r_F$ ) are usually sufficient to compute  $S_4$  to within 90% of its true value, depending on the form of the phase spectral density function (SDF) and the strength of scattering. We make initial application of the subsampling techniques to data-based phase screens for studying equatorial ionospheric scintillation with generally satisfactory results. Finally, we outline the use of the techniques developed in this paper to other practical problems, including SDF determination and computing irradiance patterns.

**INDEX TERMS:** 0669 Electromagnetics: Scattering and diffraction; 2415 Ionosphere: Equatorial ionosphere; 2439 Ionosphere: Ionospheric irregularities; 2487 Ionosphere: Wave propagation (6934); 6979 Radio Science: Space and satellite communication; **KEYWORDS:** phase screen, scintillation, ionosphere

**Citation:** Beach, T. L., T. R. Pedersen, M. J. Starks, and S.-Y. Su (2004), Estimating the amplitude scintillation index from sparsely sampled phase screen data, *Radio Sci.*, 39, RS5001, doi:10.1029/2002RS002792.

### 1. Introduction

[2] Radio signals that propagate through regions of irregular plasma density experience perturbations in amplitude and phase, i.e., scintillation. The strength of the amplitude fluctuations at a given signal frequency can often be measured directly, but to estimate the corresponding amplitude fluctuations at other, particularly lower, frequencies one must utilize the phase of the received signal. The most common method of modeling ionospheric scintillation is the phase screen [e.g., Rino,

1982], where the ionosphere is modeled as a collection of changes in signal phase at each point along the incident radio wave front. Several difficulties arise in using phase screens to model specific ionospheric conditions based on observational data. For example, information related to phase is typically available in only one dimension, whether in situ samples of plasma density along a spacecraft track [Wernik *et al.*, 1980; Franke *et al.*, 1984; Costa and Basu, 2002] or time series of phase measurements from a receiver [Beach and Kintner, 1999; Bhattacharyya *et al.*, 2000; Sokolovskiy *et al.*, 2002]. Another obstacle, and the focus of this paper, is the necessarily finite and often poor sampling resolution of the observational data.

[3] Here we investigate the practical problem of estimating the amplitude scintillation index,  $S_4$ , from sparsely sampled data for a one-dimensional (1-D) phase screen model, a case where the model can be realistically populated by 1-D observations under restricted conditions. Unlike previous analyses of phase screen data sampling and grid resolution [Buckley, 1975; Knepp, 1983; Coles *et al.*, 1995, and references therein] we do not concentrate on the best possible replication of the field in the observation plane but rather on the amplitude scintillation index itself. We present analysis based on randomly generated screens subsampled at various resolutions to find the largest sample spacing that accurately reproduces the amplitude scintillation index. We also describe subsampling curves useful for estimating  $S_4$  and develop analytic expressions for these curves in the weak scattering regime. Finally, we apply the analysis technique to in situ plasma density measurements and ground-based phase measurements in the equatorial ionosphere, where the symmetry imposed by the nearly horizontal magnetic field allows irregularities to be treated with a 1-D model when the layer thickness is sufficiently thin.

[4] The amplitude scintillation index,  $S_4$ , is defined as the normalized root-mean square (RMS) deviation of irradiance,  $I$ :

$$S_4^2 = \left( \langle I^2 \rangle - \langle I \rangle^2 \right) / \langle I \rangle^2. \quad (1)$$

Here the angle brackets  $\langle \dots \rangle$  formally denote an ensemble average but in practice indicate spatial or temporal averages. The  $S_4$  index used as the sole measure of scintillation does not parameterize phase fluctuation effects or provide detailed characterization of fade depth or duration. Also, once  $S_4$  reaches the neighborhood of unity (focusing or saturation regime), scintillation characteristics may vary even as  $S_4$  remains relatively constant. Nevertheless,  $S_4$  remains a worthwhile means of characterizing scintillation due to several factors. Large, long-term archives of  $S_4$  measurements exist and morphological studies use these archives to characterize the natural scintillation environment [cf. Aarons, 1993]. Current scintillation detection systems are based largely on  $S_4$  measurements [Groves *et al.*, 1997; Thomas *et al.*, 2001]. Additionally, scintillation at L band (1–2 GHz) or higher frequencies often does not approach saturation except in limited circumstances. Lastly, empirical relationships between  $S_4$  and properties like signal fade statistics [e.g., Fremouw *et al.*, 1980; Yeh and Liu, 1982] allow historical or climatological  $S_4$  values to be used in system design.

[5] As noted above, criteria for determining the resolution required to perform numerical phase screen computations are available. For the application at hand, the existing resolution criteria have some shortcomings,

however. Firstly, the criteria do not directly consider the computation of a statistical index such as  $S_4$  but rather the field at the plane of observation. Secondly, some of the criteria, particularly those related to the inner scale of the spectral density function (SDF) of phase fluctuations at the screen [Buckley, 1975; Knepp, 1983], are unduly conservative. One does not expect the presence or absence of very small amounts of fluctuation power above a typical, proposed inner scale's spatial frequency, where the true fluctuation power may also fall below the sensor's noise floor, to have a significant impact on scintillation. Additionally, criteria based on the RMS phase of the screen [Buckley, 1975] become ill-defined for a power law phase SDF with a poorly known outer scale, one which is often masked in detrending and other measurement-related phenomena. Low-frequency fluctuations dominate the RMS screen phase yet do not contribute much to amplitude scintillation [e.g., Forte and Radicella, 2002]. Other established criteria for phase screen application will be discussed throughout the analysis as appropriate.

## 2. Discrete Phase Screen Model and "Pinhole" Subsampling

[6] The basic scheme for the present analysis is to consider what happens to  $S_4$  as more and more samples are removed from a discrete 1-D phase screen. Conceptually, it is simpler to first investigate removing samples from the discrete sum while permitting spatial-frequency aliasing. We call this technique "pinhole subsampling" because the effect is similar to placing a screen with pinholes at regular intervals over the original phase screen. When one goes from a continuous integration to a discrete summation (i.e., a continuous Fourier transform to a discrete Fourier transform for the propagation computation) one tacitly assumes a similar discrete model, albeit one where the samples are initially very closely spaced. More realistically, sparse sensor data will have antialias filtering applied; therefore, we will subsequently examine the behavior of subsampling without aliasing.

[7] For reference, the complex amplitude of a wave at a distance  $z$  from a 1-D continuous phase screen with a normally incident plane wave above it is

$$\{A(x, z) = \frac{1}{r_F} \int_{-\infty}^{\infty} dx' A_0(x') \exp \left[ i\pi \frac{(x - x')^2}{r_F^2} \right], \quad (2)$$

where  $r_F = \sqrt{\lambda z}$  is the Fresnel radius and  $A_0(x)$  is the complex amplitude of the wave immediately below the phase screen. Figure 1 illustrates the geometry for the 1-D screen. We have ignored a phase factor of  $e^{ikz}$ , where  $k = 2\pi/\lambda$ , and a constant phase factor. Note that  $A_0(x) =$

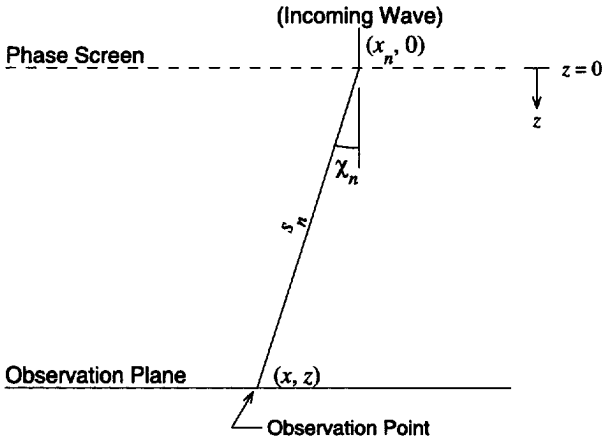


**Figure 1.** One-dimensional phase screen scattering geometry showing angle  $\chi_n$  and length  $s_n$ .

$\exp[i\phi(x)]$ , where  $\phi(x)$  is the phase of the wave front across the screen, and  $e^{-i\omega t}$  time dependence is implied. The irradiance is  $I(x, z) = |A|^2 = AA^*$  (where the asterisk denotes complex conjugation).

[8] Our starting point will be to compute the  $S_4$  for a high-resolution discrete phase screen, of sample spacing  $\Delta$ , whose irradiance pattern closely matches that of the equivalent continuous screen of equation (2). In the discrete case, we have phase samples,  $\phi_n$ , at  $x_n = n\Delta$ , with one restriction being that phase must change by less than  $\pi$  over each interval [Knepp, 1983]. Samples of the wave front immediately below the screen become  $\exp(i\phi_n)$ . Then we subsample by a factor  $\sigma$ , choosing the first of every  $\sigma$  samples according to the pinhole subsampling technique described above. This process yields a new screen whose effective sample spacing is  $\sigma\Delta$ . For the subsampled phase screen we compute the irradiance pattern at the observation plane and the resulting  $S_4$ , termed  $S_{4\sigma}$ . We compare  $S_{4\sigma}$  to the original screen's  $S_4$  (i.e.,  $S_{41}$ ) by examining their ratio as a function of  $\sigma$ , forming plots that we shall call "subsampling curves." Note that even though  $S_{4\sigma}/S_{41}$  will be seen to remain relatively constant over a wide range of  $\sigma$ , the irradiance pattern from the subsampled screen begins to deviate from that of the original screen even for small  $\sigma > 1$ .

[9] Although the discrete phase screen expressions, when appropriately simplified, are similar to the continuous case, we will present more detail than usual to emphasize the discrete nature of the calculations and because the 1-D Huygens-Fresnel formulas are not often used. Using a Huygens-Fresnel approach, we let each sample of the wave front below the screen re-radiate a cylindrical wave, as appropriate to the 1-D screen

geometry. The wave propagating from an individual element of the 1-D screen is [cf. Toraldo di Francia, 1958, pp. 355–356]:

$$V_n(x, z) = e^{i\phi_n} \frac{e^{iks_n}}{\sqrt{s_n}} \left( \frac{e^{i\pi/4}}{\sqrt{\lambda}} \frac{1 + \cos \chi_n}{2} \right) \Delta. \quad (3)$$

Here  $s_n = \sqrt{z^2 + (x - x_n)^2}$  is the distance from the point  $(x_n, 0)$  at the screen to the observation point  $(x, z)$  and  $\cos \chi_n = z/s_n$  (see Figure 1). The parenthetical terms in (3) are the obliquity factor that may be derived from Kirchhoff's scalar wave theory [e.g., Born and Wolf, 1980].

[10] The total wave field at an observation point becomes the sum of the individual wave field contributions,  $V_n$ :

$$A(x, z) = \frac{e^{i\pi/4} \Delta}{2\sqrt{\lambda}} \sum_n e^{i\phi_n} \frac{e^{iks_n}}{\sqrt{s_n}} (1 + z/s_n). \quad (4)$$

Now, we construct the following quantity based on (4) to represent the subsampled wave field:

$$A_\sigma(x, z) = \frac{e^{i\pi/4} (\sigma\Delta)}{2\sqrt{\lambda}} \sum_n e^{i\phi_{(\sigma n)}} \frac{e^{iks_{(\sigma n)}}}{\sqrt{s_{(\sigma n)}}} (1 + z/s_{(\sigma n)}). \quad (5)$$

The subsampled irradiance is  $I_\sigma(x, z) = |A_\sigma|^2 = A_\sigma A_\sigma^*$  and the normalized RMS deviation of  $I_\sigma$  gives the subsampled amplitude scintillation index,  $S_{4\sigma}$ . Except for  $I_1$ , which is essentially  $I$  as used previously, the  $I_\sigma$  have no simple physical meaning; however, the  $I_\sigma$  can be visualized readily in terms of the pinhole subsampling process. Manipulation of equation (5) provides the basis to evaluate the  $S_4$  from a subsampled screen in an efficient manner as will be seen in the next section. Note again that the phase samples are not band-limited to the new spatial Nyquist frequency when sampled at the lower rate. The extension to the band-limited case will be discussed later.

### 3. Properties of the Pinhole Subsampled Screen

[11] As outlined above, the basic quantity to investigate is  $S_{4\sigma}/S_{41}$  as a function of sample spacing. We plot these quantities against each other and examine patterns in the resulting subsampling curves for various realizations of a 1-D phase screen. Numerical experiments show that the average shape of the curve is a function of scintillation strength and the SDF of phase variations at the screen. Analytic studies confirm the dependence on the form of the SDF in the case of weak scatter and provide a quantitative basis for generalizing the results of the numerical experiments. Note that in the following

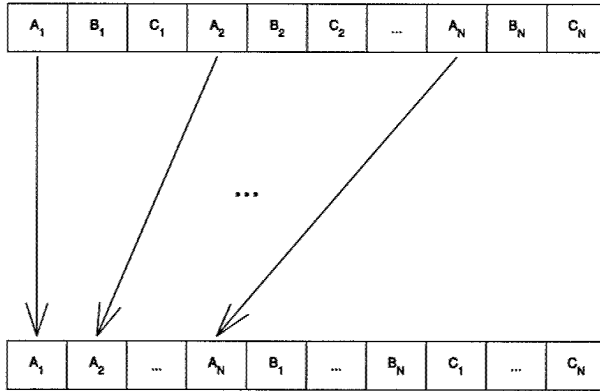


**Figure 2.** Schematic of re-packing a finite-width (but large) phase screen to perform the subsampled screen calculation. Example shown is for subsampling by a factor of 3 (i.e.,  $\sigma = 3$ ). Each set ( $A_i$ ,  $B_i$ , etc.) is termed a “subscreen” in the text.

discussion we treat the case of a phase screen with a uniform  $S_4$  across many Fresnel radii so that: (1) the screen is sufficiently wide for accurate computation [Knepp, 1983; Coles *et al.*, 1995], and (2) one can achieve a reasonably accurate estimate of  $S_4$  by averaging the variance of irradiance across the entire screen. With sparse data from real measurements maintaining a uniform  $S_4$  across many Fresnel radii is not always easy, as will be illustrated later.

### 3.1. Numerical Exploration

[12] Recalling that  $x_{(\sigma n)} = \sigma n \Delta$  and performing some algebra, we observe that equation (5) can be rewritten as follows:

$$A_\sigma = \frac{e^{i\pi/4} \Delta}{2\sqrt{\lambda/\sigma}} \sum_n e^{i\phi_{(\sigma n)}} \frac{\exp\left[i \frac{2\pi}{\lambda/\sigma} s_n(x/\sigma, z/\sigma)\right]}{\sqrt{s_n(x/\sigma, z/\sigma)}} \cdot \left[1 + \frac{z/\sigma}{s_n(x/\sigma, z/\sigma)}\right], \quad (6)$$

where  $s_n(x/\sigma, z/\sigma) = \sqrt{(z/\sigma)^2 + (x/\sigma - x_n)^2}$ . The significance of representation (6) is that it is exactly in the form of the wave field from a phase screen that uses one sample out of every  $\sigma$  samples of the original phase screen but in a new, scaled coordinate system where  $x \rightarrow x/\sigma$ ,  $z \rightarrow z/\sigma$  and  $\lambda \rightarrow \lambda/\sigma$ . This transformation is useful in efficiently calculating  $S_{4\sigma}$ .

[13] The prescription for numerical calculation of  $I_\sigma$  is to subsample the screen, scale the coordinate system appropriately and compute the field by the fast Fourier transform (FFT) technique. Using the FFT is far more

efficient than direct computation from (6), though one must be vigilant for effects due to windowing, implicit periodic continuation, etc. This numerical technique can be further improved if we recognize that there are essentially  $\sigma$  realizations of the subsampled screen present in any given realization of the original screen. We should be able to “re-pack” the original screen, if it is finite but wide, in the manner illustrated in Figure 2 to produce a new screen consisting of  $\sigma$  subscreens. Assuming minimal influence between adjacent subscreens, we can then calculate the irradiance in the scaled coordinate system and automatically average the statistics for all  $\sigma$  realizations at once by taking moments across the entire screen. This technique has the advantages of maintaining a constant FFT size (e.g., a power of 2) and providing improved statistical estimates of  $S_{4\sigma}$  for large  $\sigma$ . Appendix A investigates the effects of adjacent subscreens and other considerations and finds that the assumption made above is empirically justifiable.

[14] The phase screens that we use in the numerical experiments are of two basic types: white noise and power law screens. The white noise screen realizations consist of uncorrelated samples with Gaussian statistics. Although white noise phase screens are physically unrealistic they provide a useful analytical test. The power law screen realizations start with a white noise screen and modify its SDF to yield a power law form. To avoid low-frequency divergence problems, the power law SDF that we actually implement is constant below a cutoff spatial frequency,  $q_0$ , and proportional to the “pure” power law  $|q|^{-p}$  at higher spatial frequencies,  $q$ . Here  $p$  is the “spectral index” of the power law. Generally, we choose  $q_0$  conservatively for the power law screens so that it covers at most the two lowest frequency bins (including the zero-frequency bin) and so that  $2\pi/q_0 \gg r_F$ . For each realization, regardless of the screen type, we scale the fluctuations in the phase screen values to yield the desired starting  $S_4$  for the run.

[15] Figure 3 shows subsampling curves for numerical experiments using different 1-D phase screen realizations and various starting  $S_4$  levels. Note that the horizontal axis is the sample spacing,  $\sigma\Delta$ , normalized to the Fresnel radius,  $r_F$ . For reference, the formula for  $S_{4\sigma}$  is

$$S_{4\sigma}^2 = \langle I_\sigma^2 \rangle - 1 \quad (7)$$

when the average irradiance of the wave has been normalized to unity, as in the present case. The results presented employ the phase screen “re-packing” technique outlined above. Not shown are investigations of the Knepp [1983] criterion based on the phase change from one sample to the next. In only one case,  $p = 4$  and  $S_{41} = 0.9$ , did the RMS phase difference between subsampled points ( $\Delta\phi_{\text{rms}}$ ) exceed  $\pi$  before reaching  $\sigma\Delta = r_F$ . In all cases, this sampling criterion was satisfied

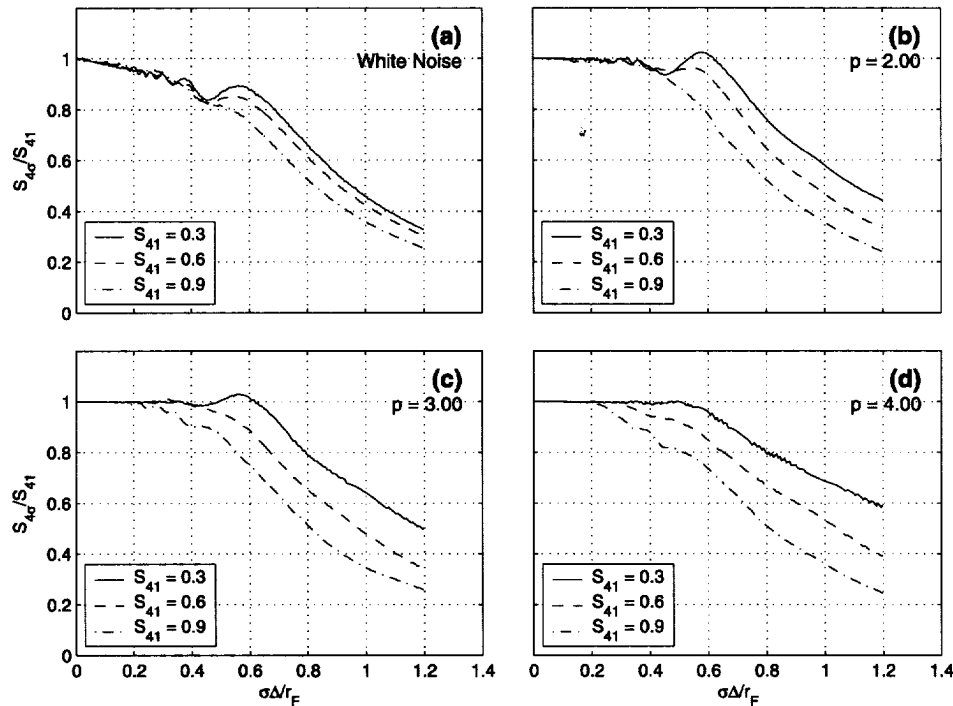


**Figure 3.** Results of numerical experiments for pinhole subsampling of random phase screens with various SDFs: (a) “white noise” (i.e., delta function ACF); (b) power law with spectral index,  $p$ , of 2; (c) power law,  $p = 3$ ; (d) power law,  $p = 4$ . These “subsampling curves” illustrate the variation of the ratio of  $S_{4\sigma}$  to  $S_{41}$ , where  $\sigma$  is the subsampling factor. The cases are selected to have  $S_{41}$  values as indicated of 0.3, 0.6, and 0.9. Computation uses the phase screen “re-packing” technique described in the text. The grid spacing of the original screen is  $\Delta$ ;  $r_F$  is the Fresnel radius. In these cases,  $\rho = r_F/\Delta = 362$  and the width of the original screen is  $181r_F$ .

for the initial phase screen (very strongly so in the power law cases) and we found no features in the curves of RMS phase difference versus  $\sigma\Delta$  that appear to indicate the structure of the Figure 3 subsampling curves.

[16] The cases in Figure 3 illustrate that a few samples per Fresnel radius are usually sufficient to compute  $S_4$  under the pinhole subsampling technique to within a few percent accuracy. More precisely,  $S_{4\sigma}/S_{41}$  remains relatively constant for the power law phase screen realizations until reaching a “knee” at a spacing between samples of about  $0.3-0.5r_F$ . Similar behavior also occurs for the white noise phase screen results, although the decrease is more pronounced prior to reaching the knee and significant “ringing” is visible to the left of the knee. In all cases shown, the behavior remains qualitatively similar over the range of starting  $S_4$  values presented and the positions of the knees move from larger to smaller spacing values with increasing scintillation strength. Figure 4 shows examples of the effects of entering the focusing and saturation regimes on subsampling curves.

Even in these strong scattering cases the subsampling curves retain forms similar to the previous ones.

### 3.2. Quantitative Analysis: Weak Scatter

[17] The general behavior of  $S_{4\sigma}/S_{41}$  with  $\sigma$ , as illustrated in these numerical experiments, is not wholly unexpected. One reasonably anticipates that the irradiance pattern of a sampled version of a continuous screen can be reproduced at a fine enough grid spacing. Although the accuracy of the reproduction will suffer at larger and larger grid spacings, most of the fluctuation power lies in the longer wavelength scales. Nevertheless, it is desirable to have a quantitative theory that explains the features of the subsampling curves. In this section we develop a theory of subsampling curves for weak scatter by considering the effects of aliasing in a continuous phase screen model.

[18] The SDF of phase is the Fourier transform of the autocorrelation function (ACF),  $\Phi_\phi(q) = F\{\langle\phi(\xi)\phi(\xi + x)\rangle\}$ . For weak scatter, a well-known result is that the

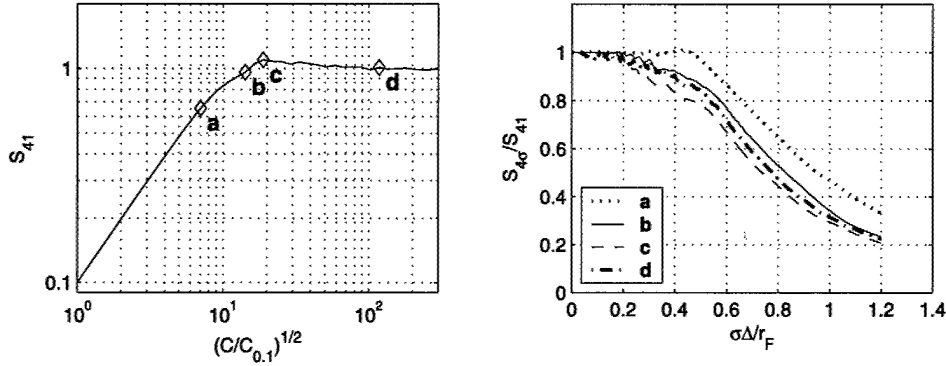


**Figure 4.** Effects of saturation and focusing conditions on pinhole subsampling results. The left-hand plot shows  $S_{41}$  as a function of SDF scaling factor  $C$ , normalized to  $C_{0.1}$ , the scaling required to yield  $S_{41} = 0.1$ . The phase screen has a  $p = 3$  power law, scaled from a new realization but otherwise having the same length and outer scale as Figure 3. Before subsampling, screens at all scattering strengths computed satisfy the Knepp [1983] Nyquist criterion (see text). The right-hand plot shows subsampling curves at the lettered points identified in the left-hand plot. For example, point “c” is the focusing peak.

SDF of irradiance variations at the observation plane is given by:

$$\Phi_{\Delta I}(q) = 4\Phi_{\phi}(q) \sin^2 \left( \frac{q^2 r_F^2}{4\pi} \right). \quad (8)$$

The subscript notation,  $\Delta I$ , emphasizes that (8) represents the Fourier transform of  $\langle I(\xi)I(\xi + x) \rangle - 1$  [Salpeter, 1967], rather than the transform of the irradiance ACF itself. The  $S_4$  value that is calculated from weak-scatter theory is then  $S_4 = U$ , where

$$U^2 = 4 \int_{-\infty}^{\infty} dq \Phi_{\phi}(q) \sin^2 \left( \frac{q^2 r_F^2}{4\pi} \right). \quad (9)$$

[19] To model the effects of subsampling we treat the discrete phase screen of equation (6) as if it adequately represents a continuous phase screen whose properties are related to the original screen. Thus for the weak-scatter case we examine what happens to equation (9) as the screen is transformed and make quantitative comparisons to the numerical results. The effects we consider in the calculation of  $U$  are: (1) subsampling and (2) coordinate scaling. Uniformly subsampling the phase ( $x_n \rightarrow \sigma x_n$ ) makes  $\Phi_{\phi}(q) \rightarrow \sigma^{-1} \Phi_{\phi}(q/\sigma)$  by the scaling theorem for Fourier transforms. Similarly, the coordinate transformation ( $x \rightarrow x/\sigma$ , etc.) makes  $\Phi_{\Delta I}(q) \rightarrow \sigma \Phi_{\Delta I}(\sigma q)$ . Note that  $q^2 r_F^2 \rightarrow (\sigma q)^2 (r_F/\sigma)^2 = q^2 r_F^2$ ; i.e., the transformation due to coordinate scaling leaves the argument of the  $\sin^2$  term unchanged. The net effects of these two transformations appear to cancel until aliasing of the SDF is considered.

[20] To account for aliasing of the SDF we adopt the following prescription. First, we limit the range of integration in (9) to the Nyquist frequency limits,  $\pm\pi/(\sigma\Delta)$ . Then the spectral density that originally covered the frequency range  $\pm\pi/\Delta$ , the initial Nyquist limits, is “folded” and summed according to the aliasing process (Figure 5) to produce a new phase spectrum,  $A_{\sigma}\{\Phi_{\phi}(q)\}$ , where the notation indicates an “aliasing functional” (the convolution of the original SDF with a periodic train of delta functions of spacing  $2\pi/(\sigma\Delta)$ ). If we denote as  $\hat{U}_{\sigma}$  the estimate of  $U$  produced by subsampling the screen,

$$\hat{U}_{\sigma}^2 = 4 \int_{-\pi/\sigma\Delta}^{\pi/\sigma\Delta} dq A_{\sigma}\{\Phi_{\phi}(q)\} \sin^2 \left( \frac{q^2 r_F^2}{4\pi} \right). \quad (10)$$

For a screen with a delta function ACF we can readily evaluate (10) and compare the theoretical results to the numerical results.

[21] For a discrete realization of delta function correlated screen, the starting SDF is  $\Phi_{\phi}(q) = k'$  (i.e., “white noise”), up to the initial Nyquist frequency,  $q = \pi/\Delta$ . In this case,  $A_{\sigma}\{\Phi_{\phi}(q)\} = \sigma k'$ . Substituting into (10) we evaluate and obtain

$$\hat{U}_{\sigma}^2 = 8k'\sigma \int_0^{\pi/\sigma\Delta} dq \sin^2 \left( \frac{q^2 r_F^2}{4\pi} \right) = 4\pi k' \left[ \frac{1}{\Delta} - \frac{\sigma}{r_F} C \left( \frac{r_F}{\sigma\Delta} \right) \right], \quad (11)$$

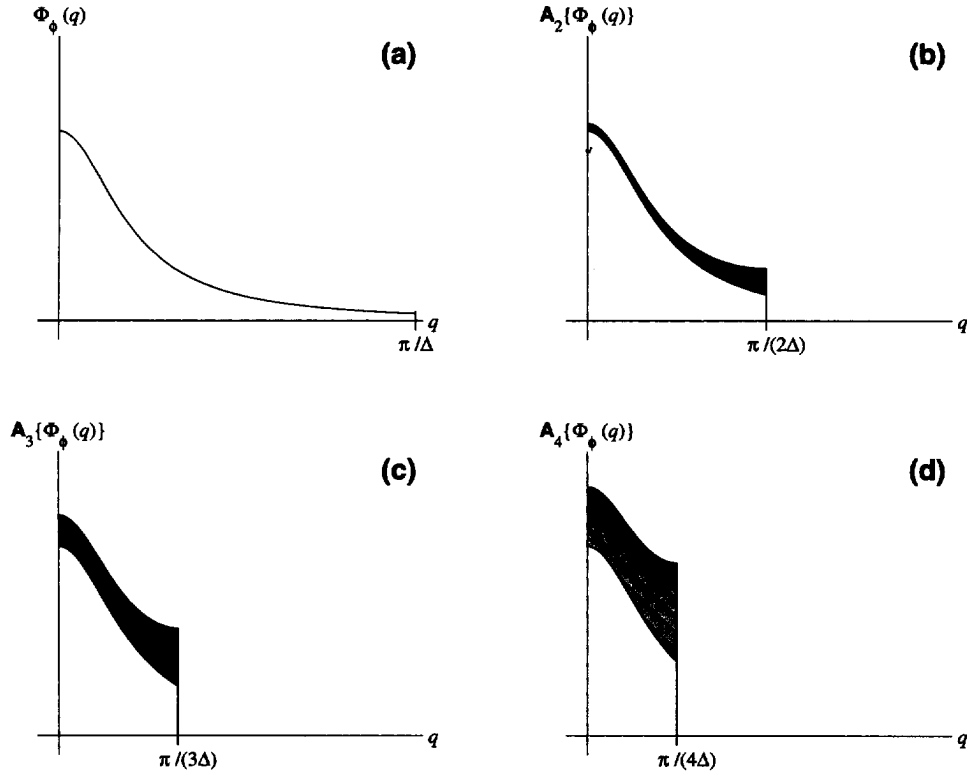


**Figure 5.** Graphs illustrating the aliasing of the SDF at different sample spacings. (a) Original SDF (schematic example, one-sided). Note that power beyond  $q = \pi/\Delta$  is assumed to be negligible. (b–d) Aliased SDF used in integral (10) for  $\sigma = 2, 3, 4$ . The range of  $q$  values is restricted to the one-sided limits of integration (i.e., 0 to  $\pi/(\sigma\Delta)$ ). The distinct shaded regions represent different portions of the original SDF that are “wrapped around” and summed to yield the overall aliased SDF,  $A_\sigma\{\Phi_o(q)\}$ .

where  $C(x) = \int_0^x dt \cos(\pi t^2/2)$  is the Fresnel cosine integral (in the form of *Abramowitz and Stegun* [1972, 7.3.1, p. 300]). For comparison with the subsampling curves in the weak-scattering case, we examine the behavior of the following expression:

$$P_\sigma = \frac{S_{4\sigma}}{S_{41}} = \sqrt{\frac{\hat{U}_\sigma^2}{\hat{U}_1^2}} = \sqrt{\frac{\rho - \sigma C(\rho/\sigma)}{\rho - C(\rho)}}, \quad (12)$$

where  $\rho = r_F/\Delta$ , the Fresnel radius normalized to the original sample spacing. Figure 6a compares the equation (12) results with the pinhole subsampling numerical results for a white noise screen with  $S_4 = 0.1$ . Note the excellent agreement between the two curves.

[22] Now we turn to a power law phase screen model [*Rino*, 1979 and references therein; *Yakushkin*, 1996, and references therein]. For the analytic approximation we take the 1-D SDF of the screen phase to be a pure (i.e., “scale-free”) power law

$$\Phi_\phi(q) = C|q|^{-p}. \quad (13)$$

The parameters  $C$  (a normalization factor related to fluctuation strength) and  $p$  (the “spectral index”) fully characterize the phase SDF. An outer scale wave number,  $q_0$ , can also be introduced but it is ill-defined in observational  $F$  region data [*Rino and Liu*, 1982]. Using a scale-free power law approximation will not significantly change computed  $S_4$  if  $\ell_0 = 2\pi/q_0$  is sufficiently large compared to  $r_F$  [*Rumsey*, 1975]. Establishing an outer scale is also not required to



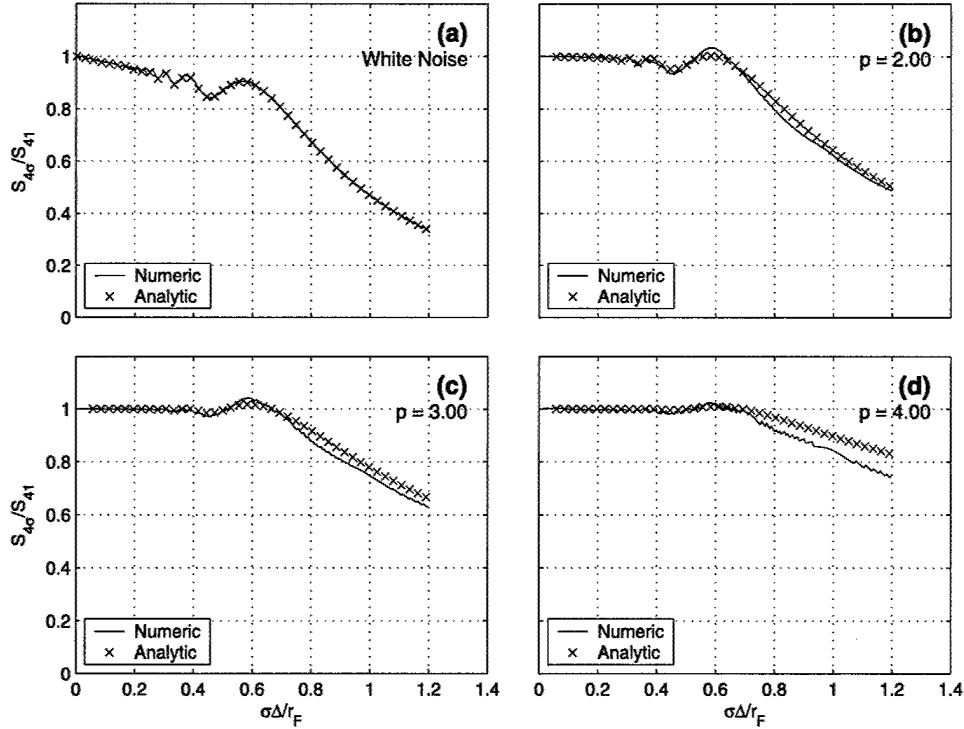


**Figure 6.** Numerical experiments in the same format as Figure 3 with overlaid analytic results from equation (12) or (15), as appropriate. Numeric subsampling results are for cases with  $S_{41} = 0.1$ . All computations have  $\rho = r_F/\Delta = 362$ . Numerical experiments have original screen width of  $181r_F$ , as before.

insure convergence in weak-scatter  $S_4$  calculations; for the SDF specified by (13), the integral (9) can be evaluated if  $1 < p < 5$ . We shall also assume that the spectral density is negligible beyond  $q = \pm\pi/\Delta$ , i.e., for small-scale sizes, so that the initial SDF can be effectively truncated to these limits without introducing significant error.

[23] To evaluate  $A_\sigma\{\Phi_\sigma(q)\}$  in the power law case we “fold” the spectrum and evaluate the results numerically. First, we simplify equation (10) with an elementary change of variables:

$$\hat{U}_\sigma^2 = 8C \left( \frac{2\sqrt{\pi}}{r_F} \right)^{1-p} \int_0^{\sqrt{\pi}\rho/2\sigma} dq A_\sigma\{|q|^{-p}\} \sin^2(q^2), \quad (14)$$

where  $\rho = r_F/\Delta$  as before. Qualitatively speaking, the potential for a knee to develop is clear from (14). Once the range of integration falls far enough inside the first maximum of  $\sin^2(q^2)$  at  $\sigma\Delta/r_F = \sqrt{2}/2 = 0.7$  the value of  $\hat{U}_\sigma^2$  drops off with increasing  $\sigma$ , if the decrease as  $q^4$

dominates the buildup of the aliased SDF. Quantitatively, forming the ratio (12) yields

$$P_\sigma = \frac{\left[ \int_0^{\sqrt{\pi}\rho/2\sigma} dq A_\sigma\{|q|^{-p}\} \sin^2(q^2) \right]^{\frac{1}{2}}}{\left[ \int_0^{\sqrt{\pi}\rho/2} dq A_1\{|q|^{-p}\} \sin^2(q^2) \right]^{\frac{1}{2}}} \approx \left[ \frac{-2^{(5-p)/2}}{\Gamma(\frac{1-p}{2}) \cos\left(\frac{(1-p)\pi}{4}\right)} \int_0^{\sqrt{\pi}\rho/2\sigma} dq A_\sigma\{|q|^{-p}\} \sin^2(q^2) \right]^{\frac{1}{2}}, \quad (15)$$

where  $\Gamma(\dots)$  is the gamma function. The approximation assumes  $\rho$  is sufficiently large so that the upper limit of the integral in the denominator can be extended to  $+\infty$ . In that case, the integral in the denominator may be evaluated for  $1 < p < 5$  [Gradshteyn and Ryzhik, 1994,

3.823, p. 484]. Note that the transformation from (10) to (14) alters the wave number range so that the SDF initially covers from 0 to  $\sqrt{\pi\rho}/2$  on the positive wave number side. Then aliasing as a function of  $\sigma$  "folds" the SDF in half, thirds, etc. from there and sums the various pieces (details in Appendix B).

[24] Figures 6b–6d compare the theoretical calculations based on the SDF with numerical experiments for weak scattering ( $S_4 = 0.1$ ). The agreement at low  $\sigma$  values is good and the features of the subsampling curves line up. The discrepancies between the theoretical calculations and numerical experiments at larger values of  $\sigma$  may represent a breakdown of the weak-scatter approximation as the SDF becomes distorted by aliasing, although the difference in SDF form between the numerical experiments and the analytic expression probably contributes. Effects like spectral leakage may also come into play. Nevertheless, the theory accounts for most features of the numerical experiments in the case of weak scattering.

### 3.3. Strong Scattering Considerations

[25] As the left-hand plot of Figure 4 suggests, and *Jokipii* [1970] proves, the weak-scattering approximation continues up to a larger  $S_4$  than perhaps is commonly appreciated if the phase SDF falls off sufficiently rapidly. Approximate strong-scattering relationships between  $U$  and  $S_4$  for power law phase screens exist throughout the literature, either in the asymptotic case [*Rumsey*, 1975; *Dashen and Wang*, 1993] or for strong focusing [*Yakushkin*, 1996]. With increasing  $U$ ,  $S_4$  does not increase without bound but eventually saturates at unity, possibly passing through a maximum value greater than 1 (i.e., focusing) on its way to saturation (cf. Figure 4). *Rino* [1979] outlines the overall behavior in more detail, although his  $U$  is defined slightly differently than here. If the power law SDF remains relatively undistorted by aliasing, as it does at low  $\sigma$ , then the relationship of  $S_{4\sigma}$  to  $\hat{U}_\sigma$  may approximate the relationship of  $S_4$  to  $U$  for the given power law. Once the form of the spectrum changes significantly as the range of integration becomes small it is not clear what the relationship might become, however. Even going from an  $S_4$  of 0.1 to an  $S_4$  of 0.3 alters the subsampling curve; that is, if Figure 6 and Figure 3 ( $S_4 = 0.3$ ) numerical experiment results are overlaid they diverge at larger values of  $\sigma$ .

[26] In the absence of a more refined theoretical approach, we conclude that it is best to rely on the results of numerical experiments for guidance in cases of stronger scattering since they are relatively simple to calculate. Clearly the results of subsampling are universal for the weak-scattering theory in the sense that the form of the subsampling curve (15) depends only on the power law exponent,  $p$ , not on the specific realization of the phase screen for a given  $p$ . It is likely that this form of

universality extends to cases with larger values of  $S_4$  as well.

## 4. Incorporating Antialias Filtering

[27] Using the definitions and analysis from the pinhole subsampling technique, we can readily extend consideration to cases where antialias filtering is applied between steps. Prior to selecting one sample out of every  $\sigma$  from the original screen, we now apply low-pass filtering to the phase samples,  $\phi_n$ , to limit their fluctuation power to the new Nyquist spatial frequency,  $\pi/(\sigma\Delta)$ . Denoting these band-limited samples as  $\hat{\phi}_{(\sigma n)}$ , we use them in place of  $\phi_{(\sigma n)}$  in formulation (6) and subsequent analysis. Practically speaking, we estimate  $\hat{\phi}_{(\sigma n)}$  by averaging over the  $\sigma$  samples from  $\phi_{(\sigma n)}$  to  $\phi_{(\sigma n + \sigma - 1)}$ . Figure 7 shows the numerical results of subsampling with antialias filtering for weak ( $S_4 = 0.1$ ) and strong ( $S_4 = 0.9$ ) scattering cases. These plots illustrate a degraded ability to estimate  $S_4$  accurately from a subsampled screen, particularly for less steep phase SDFs, as is to be expected. Nevertheless, for reasonable ionospheric power spectra ( $p \geq 2.4$  or so), it appears that a sample spacing of about  $0.2r_F$  is sufficient to compute  $S_4$  to within 90% accuracy when antialias filtering is applied.

[28] To obtain analytic antialiasing estimates we remove the aliasing functional from equation (10) and carry the substitution through to equations (11) and (14). Figure 7 presents analytic estimates so derived for direct comparison with the numerical experiment results (weak scatter, thick plot line). As before, note the excellent agreement in the white noise case and very good agreement in the power law cases, provided an outer scale is now introduced into the phase SDF to better match the SDF as actually generated. The SDF form in place of expression (13) now becomes  $\Phi_\phi(q) = C(q^4 + q_0^4)^{-p/4}$ , where  $\ell_0 = 2\pi/q_0$  is the outer scale, to approximate the SDF used in the numerical generation of the phase screen.

[29] There are subtle aspects hidden in the application of sampling theory to phase screens, however. For either type of data-based phase screen model discussed in the Introduction, the quantity sampled relates directly to the phase of the screen,  $\phi(x)$ , and not to the field,  $A_0(x) = \exp[i\phi(x)]$ , immediately below the screen. On the other hand, sampling of  $A_0$ , not  $\phi$ , is what is considered in the *Knepp* [1983] sampling-based resolution criterion and the *Costa and Basu* [2002] interpolation method. A fundamental difficulty is the modulo- $2\pi$  equivalence of phase that can complicate seemingly routine analysis [e.g., *Freund and Kessler*, 1996]. Consider the following thought experiment. Take a continuous, 1-D phase screen and add  $2n\pi$  to

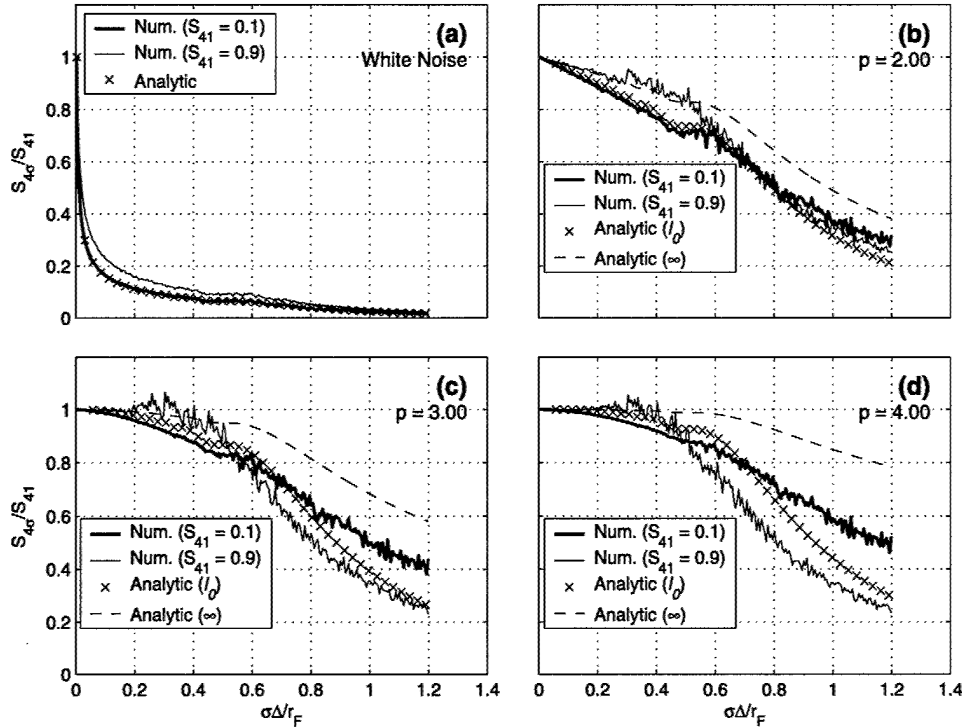


**Figure 7.** Subsampling with antialias filtering applied. Numeric (“Num.”) subsampling results are for cases with  $S_{41} = 0.1$  (weak scatter) and  $S_{41} = 0.9$  (strong scatter). Analytic estimates derive from equation (12) or (15), as appropriate, with aliasing functional removed. To obtain agreement in the power law cases, it was necessary to introduce an outer scale ( $\ell_0$ ), as is actually used in the phase screen generation, through a modification to SDF (13) that is discussed in the text. “Analytic ( $\ell_0$ )” indicates the modified SDF results ( $\ell_0 = 1.4r_F$  in this case only), whereas “Analytic ( $\infty$ )” denotes the expression (13) results (i.e.,  $\ell_0 \rightarrow \infty$ ). All computations have  $\rho = r_F/\Delta = 362$  and numerical experiments have original screen width of  $181r_F$ .

any number of arbitrary segments. Although there are technically a large number of discontinuities in the new  $\phi$ ,  $A_0$  remains identical to its previous form and the results of propagation formula (2), and its discrete equivalent, are unchanged. If, however, one applies low-pass filtering to band limit the new  $\phi(x)$  the resulting  $A_0$  will change (not as any straightforward filtering operation on the field itself) and the previously invisible phase “discontinuities” now become manifest. If  $2n\pi$  is large one can produce a tremendous amount of refractive scintillation and tailor the pattern almost at will by varying  $n$  from segment to segment and adjusting the segment widths and spacing. Similar issues arise with respect to an isolated arbitrary step in phase (not treated here).

[30] Clearly, these thought experiments possess a certain artificial character, although they bear relation to observations of dislocations in ultrasonic wave fields [Nye and Berry, 1974]. They are also inter-

twined with restrictions about permissible scale sizes of variation relative to the wavelength scale in the Huygens-Fresnel-Kirchhoff theory. At the least, these considerations indicate that some caution is warranted in the treatment of phase sampling issues. Practically speaking, such “topological” effects probably do not routinely cause serious problems under conditions where the RMS phase difference between samples is small. For example, we have found that the *Costa and Basu* [2002] technique of interpolating  $A_0$ , rather than  $\phi$ , can reproduce amplitude scintillation patterns well, despite its having problems with energy loss (interpolating the field across chords on the unit circle rather than along arcs reduces the average field amplitude). Nevertheless, we shall adopt a conservative approach pending further resolution of sampling issues. While band-limiting is unavoidable in actual data samples, we shall apply only pinhole subsampling in case studies after determining that the data lies sufficiently

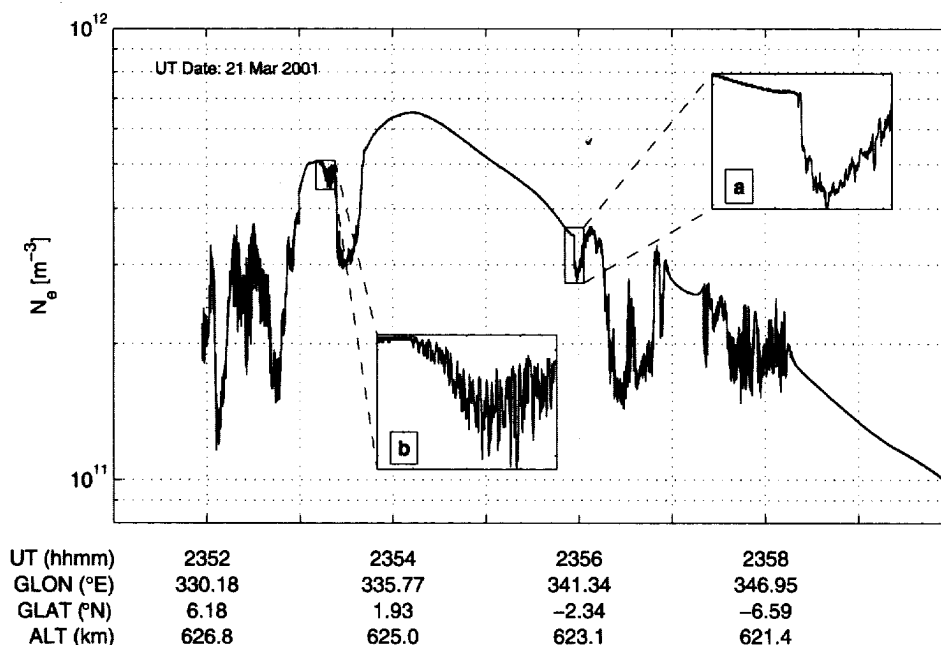


**Figure 8.** ROCSAT 1 plasma density data for 21 March 2001 (UT) with insets showing enlargements of regions under study. Magnetic local time ranges from 2210 to 2320.

far to the left on the subsampling curves,  $\Delta < 0.2r_F$ , that truncation of the SDF should have minimal effect.

## 5. Example Data Applications

[31] Now we study data-based screens to illustrate some practical subsampling issues. First, we examine high-resolution in situ plasma density data from the ROCSAT 1 satellite taken during equatorial spread *F* conditions in March 2001 near Ascension Island ( $7^{\circ}56'S$ ,  $14^{\circ}22'W$  geographic). ROCSAT 1 flies in a  $35^{\circ}$  inclination orbit near 600-km altitude and collects in situ data on ion density and drifts at a maximum rate of 1024 samples/s [Yeh *et al.*, 1999; Su *et al.*, 2001]. The effective Nyquist frequency limit depends on the local magnetic declination. For a descending pass near Ascension Island, where magnetic north lies  $17^{\circ}W$  of true north, the minimum observed scale size perpendicular to the field is approximately 9 m (4.5-m sampling). We should note for this case, and the subsequent GPS example, that the observations presented represent some of the highest resolutions available. Much of the available historical data, like the vast total electron content (TEC) data set from the International GPS Service for Geodynamics (IGS) receivers, are of significantly lower resolution [e.g., Pi *et al.*, 1997].

[32] Using the ROCSAT data-based model we mainly study the impact of “coherent” phase screen structure on the estimates of  $S_4$  obtained through subsampling. Intermittent sharp gradients in electron density tend to produce “bursty” amplitude scintillation for radio waves of a high enough frequency (e.g., GHz range) with a different distribution of amplitude fluctuations than would be found for a random screen [Wernik *et al.*, 1980; Costa and Basu, 2002]. At these higher frequencies, the Fresnel radius is less than the typical distance between sharp-gradient regions that produce most of the fluctuations in amplitude. The data-based model adopted is similar to the first model considered by Costa and Basu [2002]. This model, where the in situ data modulates the entire vertical profile, represents a worst-case scenario for the influence of coherent structures on scintillation. The model’s effect should be similar to the enhancement of scintillation observed when viewing along the magnetic field lines [e.g., Sinno and Minakoshi, 1983].

[33] Figure 8 shows ROCSAT 1 density data collected near Ascension Island on 21 March 2001. We have manually selected data regions to use in the subsampling investigation (inset enlargements). These represent data with sharp gradients (Figure 8a) and more “turbulence-like” data (Figure 8b). Even during

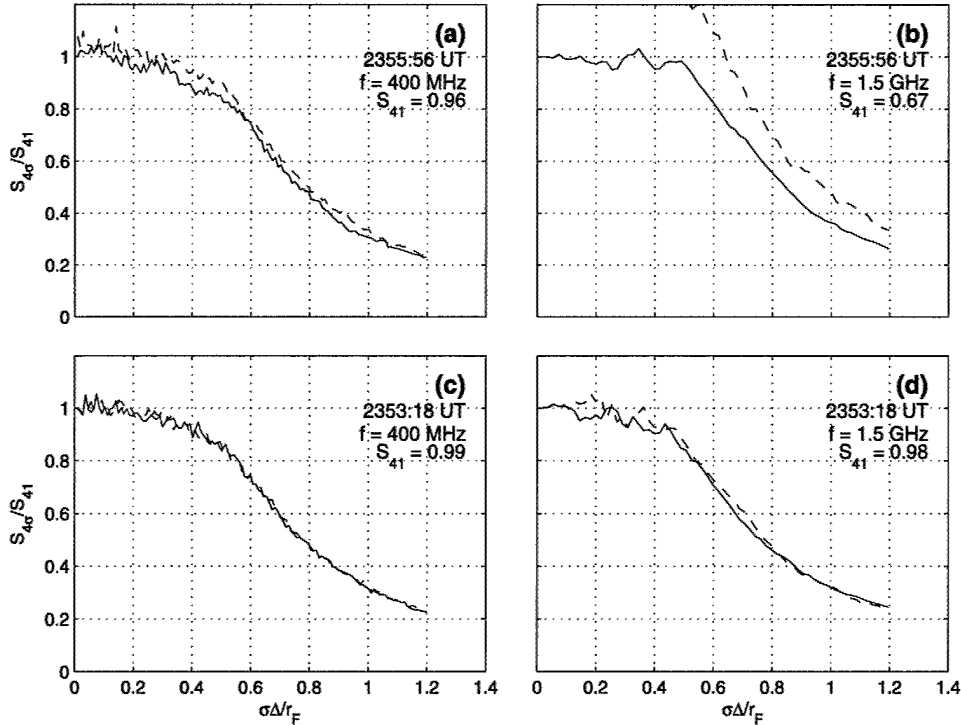


**Figure 9.** Pinhole subsampling curves for phase screens based on ROCSAT 1 data from 21 March 2001 (solid lines). The time indicated on each subplot is the start of the 2048-point (2 s) segment of plasma density data used and  $f$  is the radio frequency used. (a) and (b) Subplots from a data segment in Figure 8a. (c) and (d) Subplots from a data segment in Figure 8b. The dashed lines represent the subsampling curves for the equivalent “noncoherent” screens (see text) and have been normalized to the  $S_{41}$  values of the solid curves, not their own  $S_{41}$  values. Note that part of the dashed curve is off the scale in Figure 9b; its initial  $S_4$  value is about 1.5 times that of the solid curve.

the short data segments shown the fluctuations are clearly not statistically stationary, which is not unexpected since the satellite travels about 90 km along its track during the 12-s time periods of the enlargements. While the field at the observation plane can be computed for nonstationary fluctuations, simply using one  $S_4$  value to characterize scintillation has questionable utility in this case. Consequently, we restrict the initial phase screens prior to subsampling to have 2 s worth, or 2048 samples, of data. Since the phase screens are relatively short we must investigate screen-width concerns [Knepp, 1983; Coles *et al.*, 1995]. Also, the scatter in the  $S_{4\sigma}$  estimates will increase if fewer samples are included in the average. The data selected for the initial screens are: (1) a 2-s segment centered on the sharp edge in the Figure 8a data, and (2) a 2-s segment in the bottom of the shallow density reduction highlighted in Figure 8b.

[34] We adopt the following parameters for the satellite-derived phase screen:  $z = 308$  km with a vertical TEC

of  $3.3 \cdot 10^{17} \text{ m}^{-2}$ . These parameters are based on an ionospheric slab thickness of 100 km and digisonde measurements at Ascension Island for 2355 UT on 21 March 2001:  $\text{hmF2} = 308$  km,  $\text{NmF2} = 3.3 \cdot 10^{12} \text{ m}^{-3}$ . We take the initial spacing between sample points to be 4.5 m. Since the ROCSAT 1 data have been subjected to antialias filtering in the measurement process, spectral information perpendicular to the magnetic field at scale lengths smaller than 9 m has been lost. A 4.5-m sample spacing with the phase screen parameters above gives  $\rho = r_F/\Delta = 107$  at a radio frequency of 400 MHz and  $\rho = 55$  at 1.5 GHz. Sample spacing is thus of the order of  $0.01 r_F$  in both cases and our criterion for initially being on the left-hand side of the subsampling curves is met by an order of magnitude. The required minimum number of points,  $N$ , for adequate phase screen width is  $\sim \Delta \phi_{\text{rms}}^2 / (2\pi)$  [cf. Knepp, 1983; Coles *et al.*, 1995]. In the 400-MHz cases,  $\Delta \phi_{\text{rms}} \sim 1$  giving  $N \sim 1800$  points and indicating that a 2048-point simulation is adequate. The screen width criterion is far more strongly satisfied in the 1.5-GHz cases. Again, the

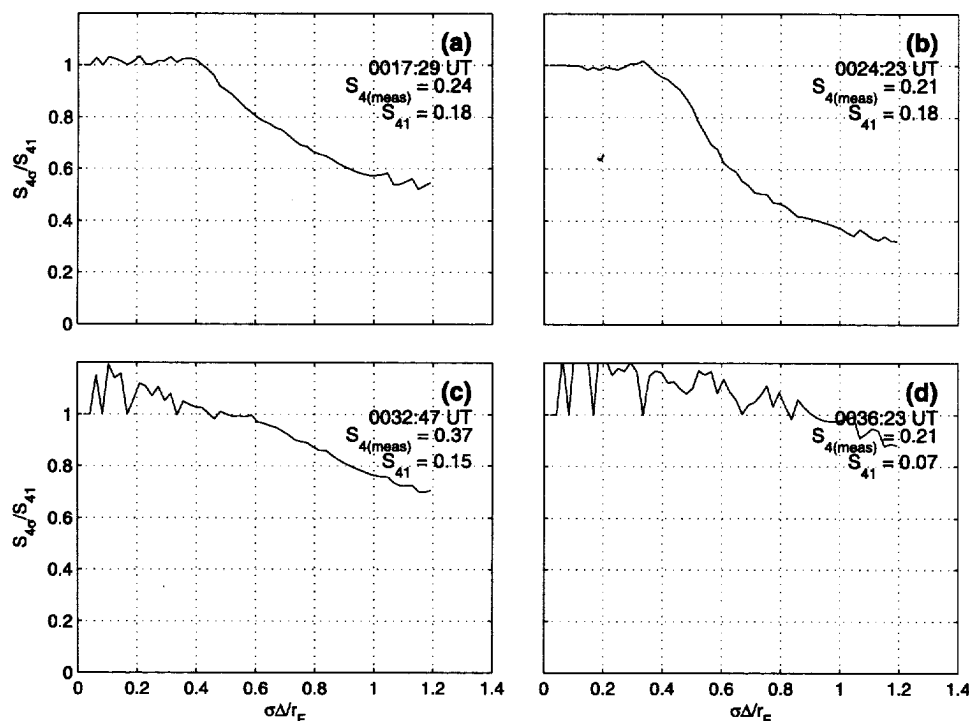


**Figure 10.** Pinhole subsampling curves for the GPS L1 frequency (1.57542 GHz) computed from GPS TEC data for satellite PRN 24 during the interval 0000–0100 UT on 8 March 2002. The computations employ 2048-point segments of 20-Hz GPS TEC data, starting at the times indicated on each subplot. We list the measured amplitude scintillation index,  $S_{4(\text{meas})}$ , from the GPS receiver for comparison. Computations are for an assumed initial sample spacing of 5 m (see text).

tradeoff in screen width for sparsely sampled real data is between stationary statistics and implicit periodic continuation effects.

[35] The solid lines of Figure 9 show pinhole subsampling curves for phase screens based on the ROCSAT 1 density data. As before, the curves show a relatively constant  $S_4$  up until a “knee” is reached as the sample spacing becomes larger. To study the effects of coherent structures we adapt a technique of *Costa and Kelley* [1978], attributed to a suggestion by D.T. Farley. In essence, we take the original phase values in our phase screen model, Fourier transform the data set, multiply each complex value by a random phase factor (uniformly distributed from 0 to  $2\pi$ ) and then transform back. The resulting phase screen should essentially have the same SDF as the original screen but with coherent structures eliminated. We repeat each of the subsampling computations shown in Figure 9 for the “noncoherent” screens generated by the above procedure and have overlaid the results with dashed lines. In three of the four cases the results are not

greatly different from those obtained from the ROCSAT 1 data directly. The exception, Figure 9b, is the case where the radio frequency is high and a particularly notable sharp gradient appears in the phase screen. A jump in phase produces a type of edge diffraction pattern and at higher frequencies the resulting irradiance fluctuations become localized below the jump, and at the ends of the screen, due to periodic continuation, unless the phases at the endpoints happen to match well (i.e., difference, modulo  $2\pi$ , close to zero). Still, in the other cases, even at a lower frequency for the same sharp gradient, the subsampling technique performs well.

[36] A different comparison may be made using GPS data, between  $S_4$  as computed from TEC fluctuations and measured  $S_4$ . We examine 20-Hz TEC and amplitude data from 8 March 2002 that were collected during an Air Force Research Laboratory (AFRL) experiment at Ascension Island with an Ashtech Z-12 receiver. The data we examine are for satellite PRN 24, which moved from north to south at an

elevation of  $55\text{--}75^\circ$  and was the closest GPS satellite to zenith during the period 0000–0100 UT under consideration. Since the satellite's line of sight moved roughly along the magnetic field and the irregularities are field aligned, as a first approximation the eastward motion of the ionosphere is the only significant contribution to changes in TEC over the short (2048-point or 102-s) intervals under study. Assuming an eastward ionospheric drift of 100 m/s yields a 5-m initial spacing between samples in the phase screen model, almost the same data spacing as for ROCSAT above. We take the phase screen distance to be 300 km.

[37] Figure 10 shows the pinhole subsampling curves and the comparison of phase screen derived  $S_4$  to measured  $S_4$  for four segments during 0012–0036 UT, the interval when moderate amplitude scintillation on PRN 24's signal occurred. Interestingly, for the cases where  $S_{41}$  is close to  $S_{4(\text{meas})}$  (i.e., Figures 10a and 10b) the subsampling curves appear more "typical" than in the remaining cases. Also, if we make the initial sample spacing smaller in the cases of Figures 10c and 10d, the computed  $S_{41}$  approaches the measured  $S_4$  and the curves become more "typical." It is possible to find values of  $\Delta$ , e.g., near 3 m, where all four curves become "typical" and the computed  $S_{41}$  is nearly the measured  $S_4$  in all cases. Thus the subsampling model appears to be capable of some success in the conversion of GPS TEC values to  $S_4$  (at the GPS L1 frequency) and might be able to yield information such as drift speed (based on sample spacing) with further refinement. We should note that we have assumed that the TEC values represent the phase of the screen directly whereas in reality the measured "TEC" consists of the true TEC value plus contributions from phase scintillation [Bhattacharyya et al., 2000].

## 6. Conclusions and Recommendations

[38] We have investigated the computation of the amplitude scintillation index,  $S_4$ , in 1-D phase screens where the sampling is sparse. Whether or not antialias filtering has been applied to the phase samples, only a few ( $\sim 5$ ) evenly spaced samples per Fresnel radius are usually necessary to compute  $S_4$  with an error of  $\sim 10\%$ . We have illustrated the application of the subsampling approach to in situ electron density data and to ground-based TEC data and conclude that the basic subsampling principles still work, although care is required for successful use. Furthermore, the novel numerical and analytical techniques that we apply to the problem show promise to address other phase screen questions.

[39] Firstly, although beyond the scope of the present work, the 2-D phase screen sampling problem needs to be addressed. Clearly, the basic framework of subsampling and aliasing considerations extends to 2-D screens quite readily. Still, the relationships among available 1-D phase data cuts [e.g., Lovelace et al., 1970], receiver time series data [e.g., Yeh and Liu, 1982] and an underlying subsampled 2-D phase screen model all need to be explored, potentially within the context of a complicated polar cap flow pattern. Secondly, the techniques have some applicability to other phase screen resolution issues, for example, the RMS error in irradiance patterns between high-resolution and low-resolution screens [cf. Coles et al., 1995]. If one splits the influence of a discrete phase screen into interspersed (pinhole-sampled) subscreens and compares the irradiance patterns, some of the autocovariance terms that appear will relate to the present results. Furthermore, the relative importance of the cross-covariance terms will likely be determined by the breakdown of  $S_{4\sigma}$  as an approximation for  $S_4$ .

[40] Follow-on work should also address the practical use of the subsampling techniques. The canonical problem is estimating lower-frequency  $S_4$  from higher-frequency phase or TEC measurements, often calibrated by  $S_4$  at the higher frequency. Subsampling curves themselves may also prove to be useful diagnostics. At the very least, they provide tests of screen generation algorithms that may skirt some of the variance issues of conventional spectral estimators. The form of the SDF determines the detailed shape of the subsampling curve and the curves with antialias filtering are particularly sensitive to the low-frequency portion of the SDF, i.e., behavior near the outer scale. Finally, another application could be deducing phase screen parameters, like drift velocity or distance, from a single GPS receiver using the subsampling curves and  $S_{41}/S_{4(\text{meas})}$  as diagnostics. As illustrated in the section on GPS results, the assumed sample spacing (related to drift) influences  $S_{41}$  and the shape of the subsampling curve.

## Appendix A: Notes on Phase Screen "Re-Packing" Technique

[41] As discussed in the text, the phase screen re-packing technique for pinhole subsampling calculations is based on the reordering of phase values illustrated in Figure 2. One concern is whether adjacent subscreens significantly influence propagation below one other and skew the value of  $S_{4\sigma}$  from the value that might be calculated from the subscreens individually. Figure A1 makes this comparison directly for representative cases and shows that the influence of adja-

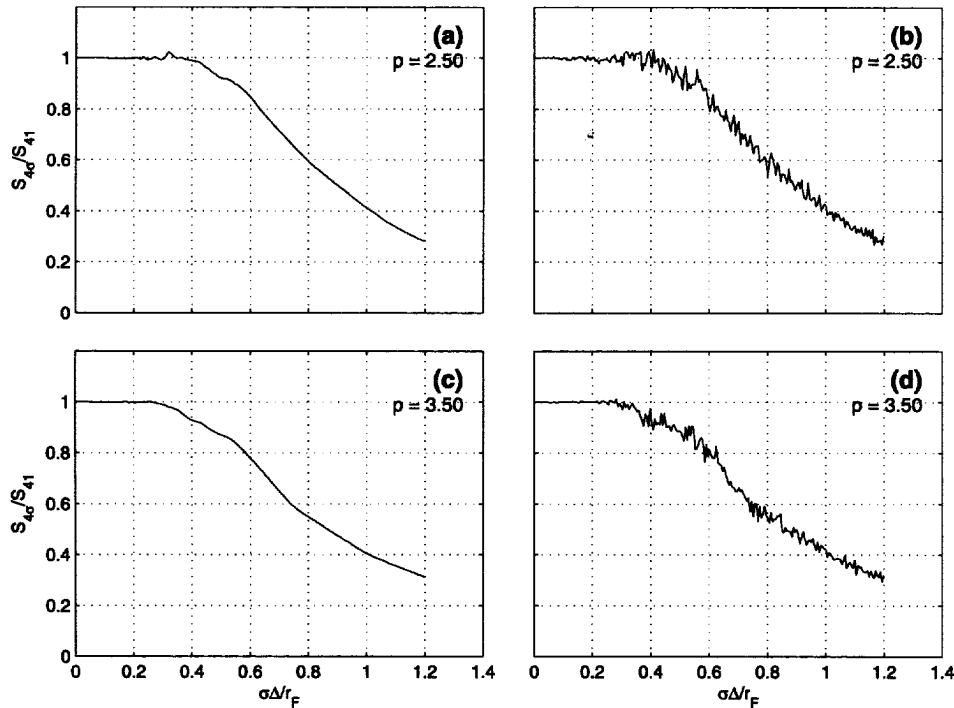


**Figure A1.** Representative comparisons of subsampling curves for phase screen re-packing technique and direct subsampling of screen for cases with  $S_{41} = 0.75$ . (a) Subsampling curve for realization of phase screen with  $p = 2.5$  as computed by re-packing technique. (b) Subsampling curve computed by direct subsampling for case 1 (Figure A1a). (c) Subsampling curve for phase screen with  $p = 3.5$  as computed by re-packing technique. (d) Subsampling curve computed by direct subsampling for case 2 (Figure A1c).

cent screens is not significant, even as  $\sigma$  becomes large. In re-packing the screen and computing the  $S_4$  across the entire screen, the ratios do tend toward the average of several of the individual subscreens; i.e., an ensemble average in the limit that the number of subscreens becomes large.

[42] The averaging inherent in the re-packing calculation raises a significant practical concern regarding the estimation of  $S_4$  from sparsely sampled phase screens, however. Specifically, in obtaining the ensemble average of the subsampling curves by the re-packing technique we have, in fact, used all of the original samples in the screen. If the variance in estimated  $S_4$  from one subscreen to the next is large then the usefulness of the subsampling technique is substantially diminished. Plots like Figures A1b and A1d provide confidence that the deviation of the  $S_4$  ratio from its ensemble-averaged value is only a few percent for any given subscreen. More analysis is required but the simple empirical investigations illustrated here are encouraging.

[43] Separate concerns relate to other practical limitations of numerical experiments, such as size restrictions on the phase screen. In the numerical experiments that are not based on observations the starting screen contains enough points to cover 181 Fresnel radii prior to subsampling. We tested the sensitivity of the numerical experiments to the ratio of overall screen size to  $r_F$  by varying the screen size. Doubling the starting screen size to  $362r_F$  and halving it to  $91r_F$  did not significantly alter the subsampling curves. Also, as discussed in the text, we found it convenient to introduce an outer scale,  $\ell_0 > r_F$ , in the generation of the power law phase screens. Additional experimentation showed that as long as  $\ell_0$  remained greater than about  $5r_F$  the influence of the outer scale on the pinhole subsampling curve was minimal.

## Appendix B: Aliasing Formulation for Power Law Screen

[44] For a given value of  $\sigma$ , the integrals (14) and (15) over the aliased SDF can be broken into  $\sigma$  parts, with the



parts summed to obtain the desired result. The integrand of the  $n$ th part is

$$D_n = \begin{cases} |q + (n-1)\delta|^{-p} \sin^2(q^2), & n \text{ odd} \\ |q - n\delta|^{-p} \sin^2(q^2), & n \text{ even,} \end{cases} \quad (\text{B1})$$

where  $\delta = \sqrt{\pi\rho}/(2\sigma)$ , the upper limit of integration, and  $n$  ranges from 1 to  $\sigma$ . We integrate each of the  $D_n$  over the interval from 0 to  $\delta$  numerically and sum the  $\sigma$  resulting values to obtain  $P_\sigma$  using (15).

[45] **Acknowledgments.** This work was supported under AFOSR Task 2311AS. The work at National Central University was supported by NSC Grant 89-NSPO (A)-PDD-008-STP01. The ROCSAT 1 data support was obtained through an AFOSR International Research Initiative (IRI) piloted by AFRL/VSBXI. We thank S. Basu and K. Groves for many helpful discussions. T. Bullett reduced the Ascension Island digisonde data for us. This research has made use of NASA's Astrophysics Data System (ADS).

## References

- Aarons, J. (1993), The longitudinal morphology of equatorial F-layer irregularities relative to their occurrence, *Space Sci. Rev.*, **63**, 209.
- Abramowitz, M., and I. A. Stegun (1972), *Handbook of Mathematical Functions*, Dover, Mineola, N.Y.
- Beach, T. L., and P. M. Kintner (1999), Simultaneous Global Positioning System observations of equatorial scintillations and total electron content fluctuations, *J. Geophys. Res.*, **104**, 22,553.
- Bhattacharyya, A., T. L. Beach, S. Basu, and P. M. Kintner (2000), Nighttime equatorial ionosphere: GPS scintillations and differential carrier phase fluctuations, *Radio Sci.*, **35**, 209.
- Born, M., and E. Wolf (1980), *Principles of Optics*, 6th ed., Pergamon, New York.
- Buckley, R. (1975), Diffraction by a random phase changing screen: A numerical experiment, *J. Atmos. Terr. Phys.*, **37**, 1431.
- Coles, W. A., J. P. Filice, R. G. Frehlich, and M. Yadlowsky (1995), Simulation of wave propagation in three-dimensional random media, *Appl. Opt.*, **34**, 2089.
- Costa, E., and S. Basu (2002), A radio wave scattering algorithm and irregularity model for scintillation predictions, *Radio Sci.*, **37**(3), 1046, doi:10.1029/2001RS002498.
- Costa, E., and M. C. Kelley (1978), On the role of steepened structures and drift waves in equatorial spread F, *J. Geophys. Res.*, **83**, 4359.
- Dashen, R., and G.-Y. Wang (1993), Intensity fluctuation for waves behind a phase screen: A new asymptotic scheme, *J. Opt. Soc. Am. A*, **10**, 1219.
- Forte, B., and S. M. Radicella (2002), Problems in data treatment for ionospheric scintillation measurements, *Radio Sci.*, **37**(6), 1096, doi:10.1029/2001RS002508.
- Franke, S. J., C. H. Liu, and J. P. McClure (1984), Interpretation and modeling of quasiperiodic diffraction patterns observed in equatorial VHF scintillation due to plasma bubbles, *J. Geophys. Res.*, **89**, 10,891.
- Fremouw, E. J., R. C. Livingston, and D. A. Miller (1980), On the statistics of scintillating signals, *J. Atmos. Terr. Phys.*, **42**, 717.
- Freund, I., and D. A. Kessler (1996), Phase autocorrelation of random wave fields, *Opt. Comm.*, **124**, 321.
- Gradshteyn, I. S., and I. M. Ryzhik (1994), *Table of Integrals, Series, and Products*, 5th ed., Academic, San Diego, Calif.
- Groves, K. M., et al. (1997), Equatorial scintillation and systems support, *Radio Sci.*, **32**, 2047.
- Jokipii, J. R. (1970), On the "thin screen" model of interplanetary scintillations, *Astrophys. J.*, **161**, 1147.
- Knepp, D. L. (1983), Multiple phase-screen calculations of the temporal behavior of stochastic waves, *Proc. IEEE*, **71**, 722.
- Lovelace, R. V. E., E. E. Salpeter, L. E. Sharp, and D. E. Harris (1970), Analysis of observations of interplanetary scintillations, *Astrophys. J.*, **159**, 1047.
- Nye, J. F., and M. V. Berry (1974), Dislocations in wave trains, *Proc. R. Soc. London A*, **336**, 165.
- Pi, X., A. J. Mannucci, U. J. Lindqwister, and C. M. Ho (1997), Monitoring of global ionospheric irregularities using the worldwide GPS network, *Geophys. Res. Lett.*, **24**, 2283.
- Rino, C. L. (1979), A power law phase screen model for ionospheric scintillation, 2, Strong scatter, *Radio Sci.*, **14**, 1147.
- Rino, C. L. (1982), On the application of phase screen models to the interpretation of ionospheric scintillation data, *Radio Sci.*, **17**, 855.
- Rino, C. L., and C. H. Liu (1982), Intensity scintillation parameters for characterizing transionospheric radio signals, *Radio Sci.*, **17**, 279.
- Rumsey, V. H. (1975), Scintillations due to a concentrated layer with a power-law turbulence spectrum, *Radio Sci.*, **10**, 107.
- Salpeter, E. E. (1967), Interplanetary scintillations, I, Theory, *Astrophys. J.*, **147**, 433.
- Sinno, K., and H. Minakoshi (1983), Experimental results on satellite scintillations due to field-aligned irregularities at mid-latitudes, *J. Atmos. Terr. Phys.*, **45**, 563.
- Sokolovskiy, S., W. Schreiner, C. Rocken, and D. Hunt (2002), Detection of high-altitude ionospheric irregularities with GPS/MET, *Geophys. Res. Lett.*, **29**(3), 1033, doi:10.1029/2001GL013398.
- Su, S.-Y., H. C. Yeh, and R. A. Heelis (2001), ROCSAT 1 ionospheric plasma and electrodynamics instrument observations of equatorial spread F: An early transitional scale result, *J. Geophys. Res.*, **106**, 29,153.
- Thomas, R. M., et al. (2001), A regional GPS receiver network for monitoring equatorial scintillation and total electron content, *Radio Sci.*, **36**, 1545.

- Toraldo di Francia, G. (1958), *La diffrazione della luce*, Ed. Sci. Einaudi, Turin, Italy.
- Wernik, A. W., C. H. Liu, and K. C. Yeh (1980), Model computations of radio wave scintillation caused by equatorial ionospheric bubbles, *Radio Sci.*, 15, 559.
- Yakushkin, I. G. (1996), Strong focusing of plane waves behind a power-law random phase screen, *Waves Random Media*, 6, 281.
- Yeh, H. C., S.-Y. Su, Y. C. Yeh, J. M. Wu, R. A. Heelis, and B. J. Holt (1999), Scientific mission of the IPEI payload onboard ROCSAT-1, *Terr. Atmos. Oceanic Sci.*, suppl., 19, 19.
- Yeh, K. C., and C. H. Liu (1982), Radio wave scintillations in the ionosphere, *Proc. IEEE*, 70, 324.
- 
- T. L. Beach, T. R. Pedersen, and M. J. Starks, Air Force Research Laboratory, Space Vehicles Directorate, Hanscom AFB, MA 01731, USA. (theodore.beach@hanscom.af.mil)
- S.-Y. Su, Institute of Space Science and Center for Space and Remote Sensing Research, National Central University, Chung-Li 32054, Taiwan.